Thrust effect in the aerodynamic sensitivity of an Ahmed body to crosswinds

Olivier Cadot[(1)], Yajun Fan[(2)], Sebastiano Fichera[(3)] and Vladimir Parézanović[(4)]

[(1)]*School of Engineering, University of Liverpool, Liverpool L69 3GH, UK, olivier.cadot@liverpool.ac.uk*

[(2)]*School of Engineering, University of Liverpool, Liverpool L69 3GH, UK, yajun.fan@liverpool.ac.uk*

[(3)]*School of Engineering, University of Liverpool, Liverpool L69 3GH, UK, sebastiano.fichera@liverpool.ac.uk*

[(4)]*Khalifa University of Science and Technology, Abu Dhabi, UAE, vladimir.parezanovic@ku.ac.ae*

ABSTRACT

A flat-backed Ahmed body equipped with passive thrust devices presents a substantial drag reduction up to 15% in crosswind. The drag reduction results from two contributions: (*i*) the thrust produced by the devices through a sailing effect and (*ii*) the base drag reduction of the body through a wake interaction mechanism. At the maximum drag reduction, the first contribution that accounts for 30% of the total drag reduction can be simply understood in the potential theory framework. The second contribution that represents 70% of the total drag reduction still remains to be understood as it involves the complex interaction between the wake devices and the full turbulent separation of the Ahmed body.

1. INTRODUCTION

Body shapes of surface vehicles are exclusively optimized for transport effectiveness, which seeks to maximise the internal volume while maintaining a compact design. These requirements are omnipresent in the transportation industries of ground vehicles (e.g. lorry trailers, minivans, SUV cars) but also of sea vehicles with their superstructure. These so-called bluff bodies, once surrounded by an airstream, develop highly complex flows featuring significant separation that ultimately is responsible for the main drag contribution (pressure drag) [1, 3]. Some aerodynamic optimisation is performed during wind tunnel tests, for given reference configurations (i.e. without crosswind), by using appendages such as spoilers and diffusers. However, the state-of-the-art remains far from satisfactory as the optimised configuration is rarely met in real conditions that, indeed, involve wide wind variations, arbitrary vehicle pitch and ground clearance [4, 2]. This is especially true in the UK due

to the high average wind intensity - of about 6.5 m/s, producing an equivalent maximum yaw of 12° at motorway speed, very likely to happen for north/south oriented routes - the highest in Europe (European wind atlas, https://www.wasp.dk/wind-atlaseuropean-wind-atlas). A yaw of 12° is associated with about 20% drag coefficient increase according to [4] who studied complex geometries.

The purpose of the present research is to take advantage of thrust effects in crosswind to obtain substantial drag reduction. Passive devices of different sizes placed on a simplified ground vehicle model are tested at different yaw of the model. In the following, the experimental set-up is firstly described in section §2, results and discussions in §3 are split into the characterisation of the baseline model in §3.1 and testing of thrust devices in §3.2. The paper is finally concluded in §4.

2. EXPERIMENTAL SET-UP

The flat-backed Ahmed model (see Fig. 1) has dimensions $L = 560$ mm, $W = 180$ mm, and $H = 200$ mm. It is supported by four cylinders of 15 mm in diameter, leaving a ground clearance of $C = 20$ *mm* at mid wheelbase (Fig. 1*a*) . The model is placed on two motorized elevators, to independently control the clearance of the front and rear axles, leading to the variation of the pitch angle α as shown in Fig. 1(*a*). This assembly is mounted on a turntable driven by a motorized rotation stage to control the yaw angle β as shown in Fig. 1(*b*).

A six-component force balance (F/T Sensor: Gamma IP65, manufactured by ATI Industrial Automation) is supporting the two elevators and rotates with the rotary stage. It measures f_x, f_y, f_z in the coordinates system $(\mathbf{e_x}, \mathbf{e_y}, \mathbf{e_z})$ of Fig. 1. Time series of the components are acquired at a sample frequency of 1 kHz. The acquisition
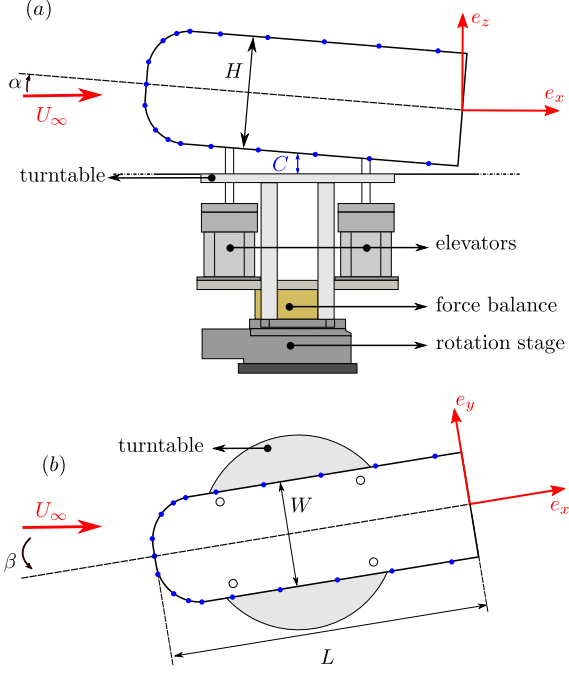
Figure 1: Side (*a*) and top (*b*) mid-section views of the flat-backed Ahmed body with pressure measurements (blue dots), force balance and the 3 degrees of freedom positioning system (elevators and rotary stage).

time is 50 s. The model frontal area $H \times W$ is used to calculate the force coefficients:

$$c_i = \frac{f_i}{q_\infty HW}, (i = x, y, z), \qquad (1)$$

where q_∞ is the dynamic pressure. The force balance resolution is 0.025 N for f_x, f_y and 0.05 N for f_z which translates in 5×10^{-3} for values of c_x, c_y and 10×10^{-3} for values of c_z presented in the paper.

The pressure is measured at 61 locations marked by blue points in Figs. 1, 2, using a Scanivalve ZOC33/64PX pressure scanner calibrated before each use with a calibrator and precision manometer (Furness Control FCO650). The sampling frequency is 1 kHz per channel with a checked accuracy of converged mean values better than ± 0.5 Pa (it translates into an accuracy of base drag coefficients in Eq. 3 to ± 0.005). The static pressure p_∞ of the test section is used to compute the instantaneous pressure coefficient :

$$c_p = \frac{p - p_\infty}{q_\infty}. \qquad (2)$$

A simple integration of the 20 pressure taps over the flat trailing edge (Fig. 2) provides the base drag coefficient

$$c_b = -\iint_{\text{base}} c_p ds \qquad (3)$$

It is the contribution of the base to the total drag coefficient c_x. The wind velocity is set to $U_\infty = 15.8$ m/s

(i.e $q_\infty = 150$ Pa), corresponding to the Reynolds number $Re = U_\infty H / \nu \approx 2.1 \times 10^5$.

We decompose the mean total drag C_x into the mean base C_b and the mean fore-base C_{fb} contributions, respectively displayed by grey and white surfaces in Fig. 2 :

$$C_x = C_b + C_{fb}. \qquad (4)$$

Thus, the fore-base contribution C_{fb} accounts for all the drag sources that are not the base drag : friction drag, pressure drag of the fore-body, the supports and any additional appendices not placed on the base. The C_{fb} value is simply computed from both the measurements of the total drag (Eq. 1) and base drag (Eq. 3).

Additional appendices to reduce drag in crosswind (i.e. $\beta \neq 0$) are placed on the rear top of the model as shown in Fig. 2(*b*). They are two identicals NACA0010 aerofoil of chord $c = 60$ mm with three possible spans, $b = \frac{1}{4}H$ (50 mm), $\frac{1}{2}H$ (100 mm), or $\frac{3}{4}H$ (150 mm).
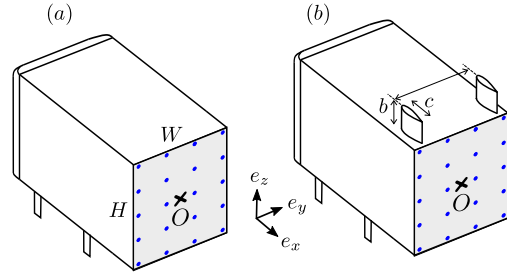

Figure 2: Baseline Ahmed body (*a*) and model (*b*) equipped with appendices (see text). The blue dots show the pressure taps locations used for the base drag evaluation in Eq. 3.

3. RESULTS AND DISCUSSIONS

3.1 Ahmed body

We first study the baseline model as drawn in Fig. 2(*a*). Force coefficients for the baseline will be marked with an additional subscript 0, such that total drag, base drag and fore-base drag are respectively C_{x_0}, C_{b_0} and C_{fb_0}. Figure 3(*a*) shows the sensitivity map of the mean drag coefficient to yaw and pitch. It can be seen that drag may be increased up to 30% for extreme yaws independently to the pitch. In contrast, sensitivity to the pitch is mainly restricted to small yaws $|\beta| < 3°$. The base drag sensitivity shown in Fig. 2(*b*) indicates increases up to approximately 100% for extreme yaws. It is clear from these two figures that at large yaw, the total drag coefficient becomes exclusively dominated by the base suction produced by the separated wake. Indeed, the fore-base contribution C_{fb_0} in Fig. 2(*c*) tends to zero at large yaw. The explanation of this fore-base drag cancelling with yaw is
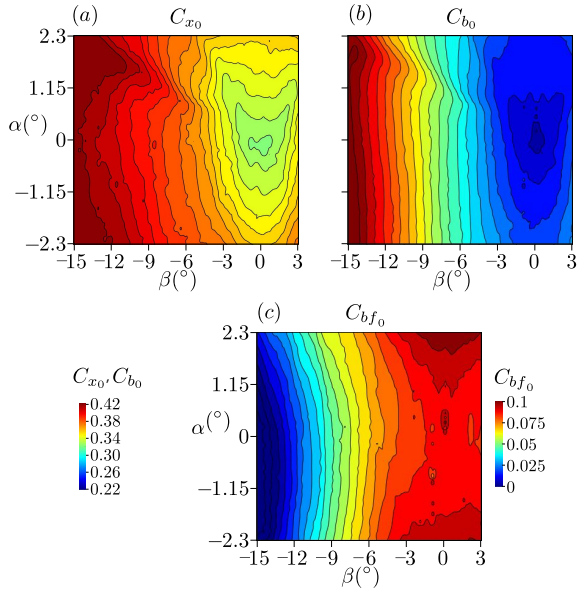
Figure 3: Sensitivity maps of drag (*a*), base drag (*b*) and fore-base drag (*c*) to yaw and pitch variations for the baseline Ahmed body.
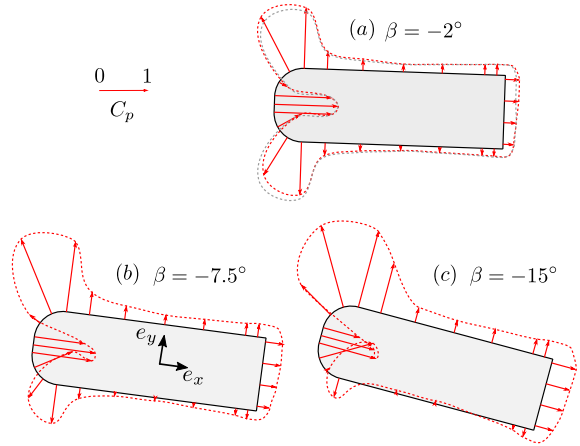

Figure 4: Pressure coefficient distribution in the horizontal mid-section at different attitudes of the baseline Ahmed body. The distribution with the body aligned ($\beta = 0°$) with the wind is displayed in grey in (*a*).

illustrated in Fig. 4 showing the mean pressure distribution at a mid-height horizontal section of the body. As the yaw is increased in Fig. 4, a low pressure region forms on the leeward side of the body nose which produces a thrust along the *x*-direction. This "sailing" effect induced by the crosswind is sufficient in strength to cancel the fore-base drag.

The sensitivity of the drag in crosswind to the flow around the fore-body is further evidenced in Fig. 5. In this experiment, additional vertical velcro stripes are placed at the centre of both circle arcs of the body nose (see Fig. 5*a*). As can be seen in Fig. 5(*b*), the presence of the stripes barely increases the drag at small yaw. In contrast, it overshoots the drag value for yaws larger than 10°. This overshoot has no relationship with the base drag that remains almost unaffected in Fig. 5(*c*) but clearly produced by a loss of fore-base thrust for $|\beta| > 10°$ as shown in Fig. 5(*d*). it is suspected that the velcro stripes trigger a separation on the leeward side of the nose that weakens the low pressure responsible for the thrust.

3.2 Ahmed body with passive thrust devices

In this section, the appendices displayed in Fig. 2(*b*) are tested on the baseline having velcro stripes (Fig. 5*a*).

Figure 6 shows the total drag and its decomposition for the baseline and the 3 different appendices sizes. We can see in Fig. 6(*b*) that the appendices are always beneficial

for the total drag. However, the hierarchy of the drag reduction amplitude with the size *b* inverts at approximately $|\beta| = \beta_{\text{inv}} \approx 8°$. For yaws smaller than this value, the larger the drag reduction, the larger the appendix while for larger yaws, the larger the drag reduction, the smaller the appendix.

We turn now to the two contributions of the total drag. The base drag in Fig. 6(*c*) is also found to be reduced but monotonously on the full range of investigated yaws. The base drag reduction is as large that the base drag or the yaw is large. In addition, there is almost not differences between the 3 tested sizes. Although the recirculating flow at the base must be modified to explain the monotonous base drag reduction with yaw, it is not responsible for the inversion seen in the total drag (Fig. 6*b*). Actually, the inversion in the drag reduction hierarchy is solely due to the fore-base drag as can be seen in Fig. 6(*d*). At zero yaw, the appendices increase the drag compared to the baseline as expected by increasing the frontal area. Yawing the model decreases rapidly the fore-base drag because of the lift produced by the appendices (here, it is a side force) which, projected on the *x*-direction, is responsible for a thrust. For the two largest appendices $b = \frac{1}{2}H$ and $\frac{3}{4}H$, this mechanism occurs when $|\beta| < \beta_{\text{inv}}$. For larger yaws, $|\beta| > \beta_{\text{inv}}$ the flow around the appendices reaches the stall thus reducing considerably the associated thrust. The stall also produces a separated drag. The drag inversion is thus simply explained by the fact that the beneficial thrust for $|\beta| < \beta_{\text{inv}}$ and the detrimental separated drag for $|\beta| > \beta_{\text{inv}}$ are both roughly proportional to the appendix span *b*. It is possible to assess the thrust produced by the appendices in the *x*-direction by subtracting the baseline fore-base drag to that of the baseline with appendices :
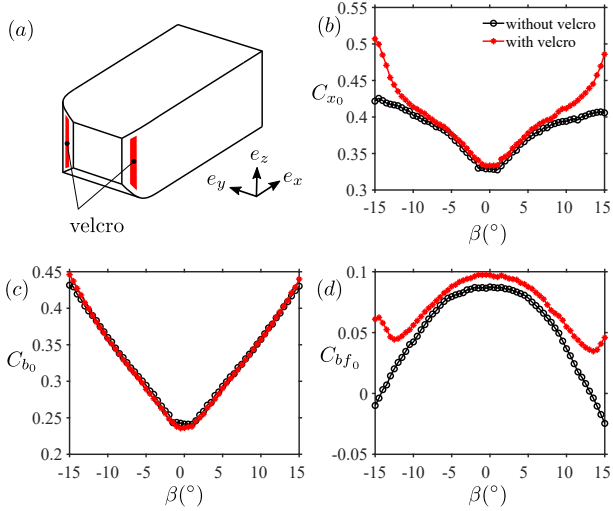
$$T \approx C_{fb} - C_{fb_0}. \tag{5}$$

3

Figure 5: Baseline model (a) at zero pitch with velcro stripes. Comparisons of drag (b), base drag (c) and fore-base drag (d) without and with velcro stripes.
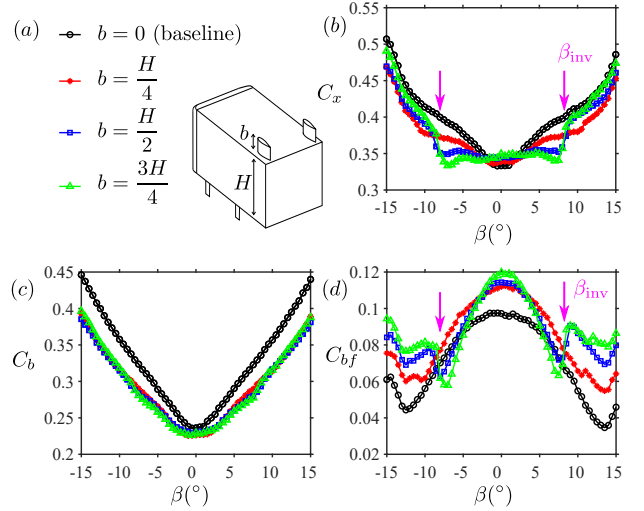

Figure 6: Ahmed body at zero pitch with passive thrust device. Comparisons of drag (b), base drag (c) and fore-base drag (d) for the baseline, $b = \frac{1}{4}H$, $\frac{1}{2}H$ and $\frac{3}{4}H$.

A negative T indicates a thrust force on the appendices, aligned with the body and orientated towards the front of the body. This estimate is shown in Fig. 7(a). Surprisingly, the smallest device with $b = \frac{H}{4}$ (red colour) never produces a net thrust before the stall (that occurs around 10°) indicating that the total drag reduction measured in Fig. 6(b) is only due to the base pressure recovery or the base drag reduction in Fig. 6(c). A net thrust is actually observed for the two taller profiles in the yaw ranges $5° < \beta < 7°$ in Fig. 7(a). It is also in these ranges that the base drag is the most reduced by the presence of the appendices as can be seen in Fig. 7(b). It is the combination of the thrust production on the appendices together with the base drag decrease that produces the largest drag reduction, up to 15% for $b = \frac{3}{4}H$ compared to the baseline in Fig. 7(c). It is worth mentioning that for a given yaw in Fig. 7, the drag reduction by thrust production shown in Fig. 7(a) is always smaller than that by base drag reduction in Fig. 7(b).

Although these devices produce interesting drag reduction in crosswinds, they unfortunately also increase the total side force and roll moment that could affect the vehicle stability by increasing its ability to skid. The side force coefficients shown in Fig. 8(a) clearly indicate such increase by the passive devices. The side force coefficient S due to the devices can actually be assessed by subtracting the baseline:

$$S \approx C_s - C_{s_0}, \qquad (6)$$

as shown in Fig. 8(b). For comparison, we compute the theoretical side force coefficient produced by two thin aerofoils of surface bc at an angle of attack β in a uniform flow U_∞ obtained from the potential flow theory :

$$S_t = 2 \times \frac{1}{q_\infty HW} L \cos\beta, \;\; L = -q_\infty(bc)2\pi \sin\beta \quad (7)$$

The dashed line in Fig. 8(b) represents this theoretical value as $\frac{H}{b} S_t$. It compares fairly well at first order to the experimental data as long as $\beta < \beta_{\text{inv}}$, despite the different boundary condition at the edges and the non uniformity of the incoming flow.

4. CONCLUSION

We have shown that an Ahmed body equipped with vertical wings present a substantial drag reduction in crosswind, up to 15% for a yaw around 7°. The drag reduction results from the thrust produced by the wings through a sailing effect and the base drag reduction of the body through a wake interaction mechanism. While the first contribution can be simply understood in the potential theory framework, the second contribution requires more investigations about the flow field especially since it represents 2/3 of the drag reduction at 7°. It would also be interesting to extend the yaw range of effective drag reduction, that is limited to 7°, with a better design of the thrust device and to study a solution to keep the side force coefficient to acceptable values for the vehicle stability.

REFERENCES

[1] S.R. Ahmed, G. Ramm, and G. Faitin. Some salient features of the time-averaged ground vehicle wake.
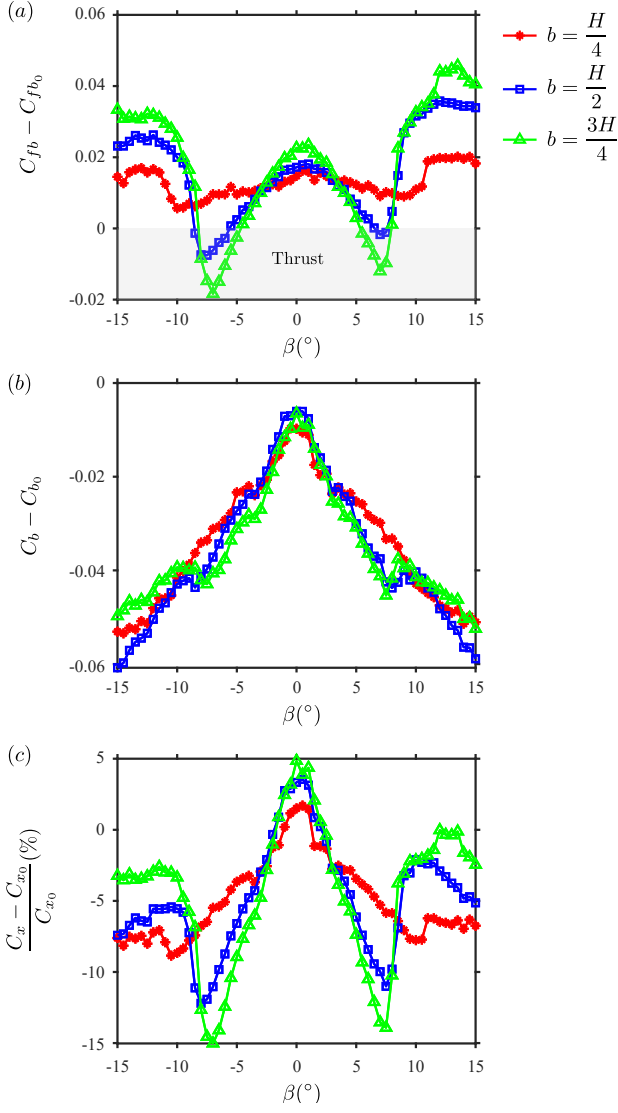
Figure 7: Ahmed body at zero pitch with passive thrust device. Variations from the baseline of drag (*b*), base drag (*c*) and fore-base drag (*d*) for $b = \frac{1}{4}H$, $\frac{1}{2}H$ and $\frac{3}{4}H$.

Figure 8: Side force coefficient for the four tested model (*a*) and its variation from the baseline scaled by $\frac{H}{b}$ (*b*) for $b = \frac{1}{4}H$, $\frac{1}{2}H$ and $\frac{3}{4}H$. The dashed line is $\frac{H}{b}S_t$ as defined in Eq. 7.

SAE Technical Paper Series, 840300, 1984.

[2] G. Bonnavion, O. Cadot, V. Herbert, S. Parpais, R. Vigneron, and J. Délery. Asymmetry and global instability of real minivans' wake. *Journal of Wind Engineering and Industrial Aerodynamics*, 184:77–89, 2019.

[3] H. Choi, J. Lee, and H. Park. Aerodynamics of heavy vehicles. *Annual Review of Fluid Mechanics*, 46:441–468, 2014.

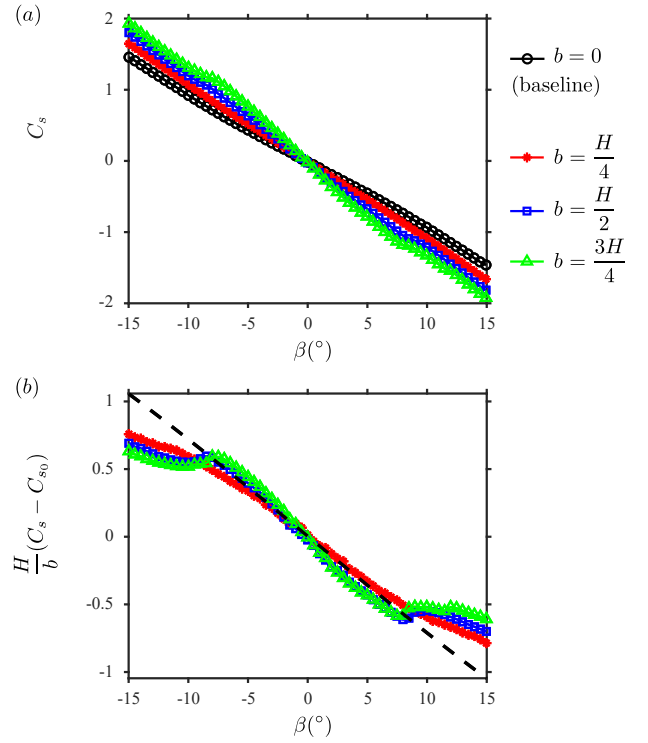[4] J. Howell. Aerodynamic drag of passenger cars at yaw. *SAE International Journal of Passenger Cars-Mechanical Systems*, 8(2015-01-1559):306–316, 2015.